Technologies and Materials for Renewable Energy, Environment & Sustainability

Preparation of Novel Hybrid Polymeric Coatings for Corrosion Protection of Steel Rebars

AIPCP25-CF-TMREES2025-00071 | Article

PDF auto-generated using **ReView**
from
RIVER VALLEY
TECHNOLOGIES

Preparation of Novel Hybrid Polymeric Coatings for Corrosion Protection of Steel Rebars

Sawsan H. Alwan[1,] and Ali S. Ismail[1,a)]

[1] *Department of Chemistry, College of Education for Pure Sciences, University of Anbar, Ramadi city, Iraq*

[a)] *Corresponding author: esp.ali.sami@uoanbar.edu.iq*

Abstract. In this study, an organic–inorganic hybrid polymer for the corrosion protection of steel rebars was prepared from ethyl methacrylate, 3-(trimethoxysilyl)propyl methacrylate (TMPSM), through free-radical polymerisation using different molar ratios of benzoyl peroxide as the initiator. The samples were denoted as W1, W2, and W3. Following acidic hydrolysis and condensation of tetraethyl orthosilicate with the TMPSM using the sol-gel process, both solutions were then mixed to obtain a hybrid polymer matrix containing both organic and inorganic phases. Subsequently, steel reinforced coatings demonstrated the highest adhesion levels during adhesion tests. The hybrid polymer films were then characterised using Fourier transform infrared spectroscopy to confirm their skeletal structures. The structural features of the hybrid polymeric coatings were investigated using ^{1}H and ^{13}C NMR spectroscopy, and the overall impacts of structure on the thermal behaviour and thermal transformation were examined using thermogravimetric analysis and differential scanning calorimetry methods, while the surface and morphological characteristics of the corrosion product films were examined using SEM and AFM. The results showed that the coatings were similar in terms of surface topography, verifying their nanoscale distribution (18–200 nm particle size).

Keywords: Organic–inorganic hybrid polymer, sol-gel process, corrosion protection, ethyl methacrylate, steel rebars

INTRODUCTION

Since 1854, reinforcing steel—also known as reinforcing bars—have been incorporated into structural and architectural designs in France; following the widespread use of structural concrete, steel or reinforcing bars were considered complementary to it, with the presence of steel within the concrete mass serving as the material that could resist tensile stresses, whereas the concrete resisted compressive stresses. Since then, concrete without steel reinforcement has been considered to have low tensile strength [1]. Nonetheless, steel corrosion within reinforced concrete structures [2,3] has become a challenging and common problem for engineers and architects; moreover, the early deterioration within reason steel corrosion now represents a serious threat to the quality of concrete as the primary material used in infrastructure construction. Corrosion damage has become a major problem, related, as it is, to public safety, technical, economic, and environmental concerns. The corrosion of reinforcing steel begins when concrete is exposed to various processes that lead to an oxide layer forming on the steel surface within the concrete, especially the steel close to the surface of the concrete, owing to changes in the concrete's pH. Subsequently, chloride ions can infiltrate the concrete, creating a negative layer that displaces the protective layer and inhibits anodic decomposition of the steel [4,5]. Here, metals such as iron, aluminium, titanium, copper, magnesium, and their alloys undergo metallic corrosion owing to chemical reactions between the environment and metal surface, which transform the metal back into its original stable ore state. In the case of steel and aluminium, Cl^{-}, O_2, and H_2O species can trigger the transfer of electrons and are the primary cause of corrosion [1,2].

Over the past few years, the preparation and production of sol-gel coatings that can reduce and delay corrosion have been studied. These hybrid organic–inorganic coatings are representing a new era of multifunctional materials with a variety of applications and useful features. The sol-gel process [6–8] allows for the deposition of coatings on reinforced steel with different spots using simple and inexpensive equipment at low temperatures with readily available organic solvents [9–12]. More importantly, the sol-gel process provides excellent control over the volumes and quantities of the starting compounds, ease of composition modification, and the potential to introduce functional groups [12]. represent a new era of multifunctional materials. Methyl methacrylate (MMA) was the first commonly

used organic compound; it is a non-toxic, colourless, transparent monomer that is widely used in various commercial applications [13,14], and is considered to be the organic phase in most of hybrid coatings. The corresponding silicon alkoxides (silanes) produce silanol groups Si–OH, one of the monomers of which is 3-methacryloxypropyltrimethoxysilane (MAPTMS), in addition to inorganic silicon, such as tetraethyl orthosilicate (TEOS) which contains alkoxide groups, which are considered to be the inorganic phase, and it can be polymerized with organic monomers as an organic phase to produce hybrid materials with good adhesion to reinforced steel [14–18]. The polymerisation of organic and inorganic monomers can be conducted sequentially [19,20]. Organic polymerisation—conducted in the organic phase—results in the formation of linear polymers or copolymers. Inorganic monomers are incorporated during the inorganic phase—either within the polymer backbone or at the chain ends—as observed in the 3-(trimethoxysilyl)propyl methacrylate (MPTS) monomer [21,22]. Hydrolysis and condensation reactions, the degree of polymer branching, and the homogeneity of the gel determine the final chemical and physical properties of the organic–inorganic hybrid coatings [23,24]. Homogeneous gel materials are typically free of defects. For the efficient drying of the hybrid films and removal of by-products and water during the gel hardening process, the organic-inorganic hybrid corrosion-resistant coatings are prepared using the sol-gel process. After the evaporation of alcohol and water, the remaining Si–OH groups in the siloxane network within the absorbent layer (Si-O-Si) hinder the penetration of water, oxygen, and chloride ions as corrosion agents [25–27]. In this study, an organic–inorganic hybrid polymer was prepared using ethyl methacrylate (EMA) and TMPSM monomers and benzoyl peroxide (BPO) as an initiator through free-radical polymerisation (PEMA/TMPSM) as the organic phase, followed a sol-gel method based on the polymerisation of tetraethyl orthosilicate (TEOS) and 3-(trimethoxysilyl)propyl methacrylate (TMPSM) to form (TEOS/ TMPSM) as the inorganic phase. The TMPSM monomer forms covalently bonded inorganic and organic phases as a coupling agent. In this context, the volume ratios of EMA/ TMPSM and TEOS/ TMPSM were kept constant, while the ratios of the three BPO initiators were modified. The three hybrid polymers prepared were denoted W1, W2 and W3. The thermostability and structure of the hybrid coating polymers W1, W2, and W3 were studied using Fourier transform infrared (FT-IR) spectroscopy, nuclear magnetic resonance (NMR, ^{1}H and ^{13}C) spectroscopy, thermogravimetric analysis (TGA), and differential scanning calorimetry (DSC). The morphological characterisation and coating thicknesses of the three hybrid polymers were measured using scanning electron microscopy (SEM) and atomic force microscopy (AFM).

EXPERIMENTAL METHODS

The reagents used in this study were ethyl methacrylate ($C_2H_5O_2CC(CH_3)=CH_2$) (EMA), 3-trimethoxysilyl)propyl methacrylate ($CH_2=C(CH_3)COO(CH_2)_3Si(OCH_3)_3$ (TMPSM), tetraethyl orthosilicate ($Si(OCH_2CH_3)_4$ (TEOS), benzoyl peroxide ($C_6H_5–C(=O)O–)_2$ (BPO), and ethanol CH_3CH_2OH, (Sigma–Aldrich). All materials were of laboratory grade and used as received. The FT-IR spectra (500–4000 cm^{-1}) were obtained using a Tensor 27 Bruker spectrophotometer on synthesised films; the ^{1}H and ^{13}C NMR spectra were obtained using a Bruker Ascend 400 MHz device; the TGA/DSC curves of the hybrid films were obtained using a Mettler-Toledo device, under atmospheric air conditions and without a purging gas. The samples were heated from 25 to 518 °C and the surface morphology was characterised using SEM (TESCAN Vesga 3 SBH, 3.0 kV). Finally, AFM measurements were performed using an AFM/SPM DualScope device. First, the monomer (8.20 mL of EMA) with 3-(trimethoxysilyl)propyl methacrylate (2.50 mL of TMPSM) were polymerised in 25 mL of ethanol, using a molar ratio from the thermal initiator (0.025 (0.33 gm) of BPO). The reaction was conducted under constant stirring in a reflux flask over a 4 h period at 80 °C. The polymerisation of the other hybrid polymers was performed using the same approach, but the volumes were kept constant, while the BPO initiator ratios were varied. The initiator molar ratios were (0.05 (0.66 gm) of BPO) and (0.1 (1.32 gm) of BPO) and the three hybrid polymers prepared were denoted as W1, W2 and W3, respectively. The polymerisation mechanism is as shown below [28–31].

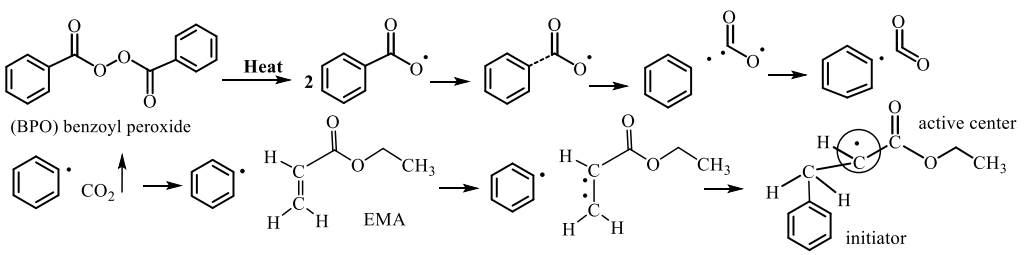

Next, the inorganic monomer 3-(trimethoxysilyl)propyl methacrylate (MPTS), which contained the acrylic end, was added by injection [28].

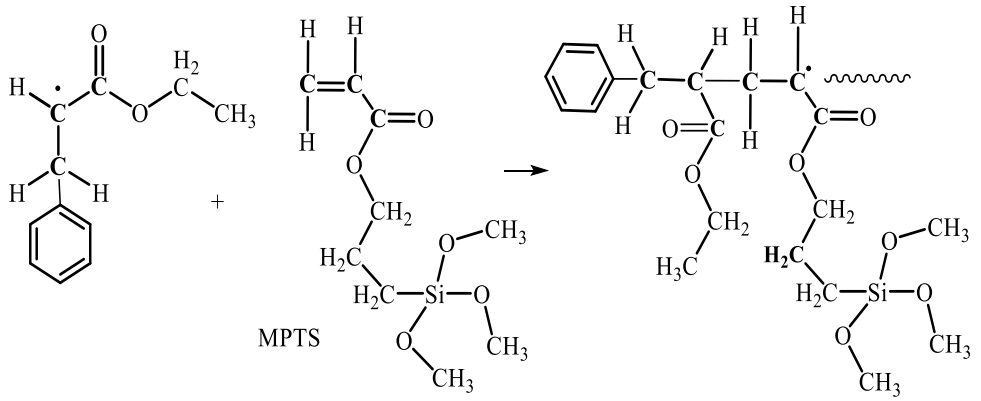

The product obtained was kept until completion of the second stage, which was hydrolysis and condensation. Here, in a separate step, the inorganic polymer was prepared by the hydrolysis and condensation (sol-gel reaction) of silicon alkoxide (4.5 mL of TEOS) with (2.5 mL of TMPSM). The TEOS was hydrolysed in an ethanol solution with acidified water (3.00 mL ethanol, 2.00 mL H_2O) using drops of nitric acid for 1 h at 25 °C under constant stirring in a closed flask [28].

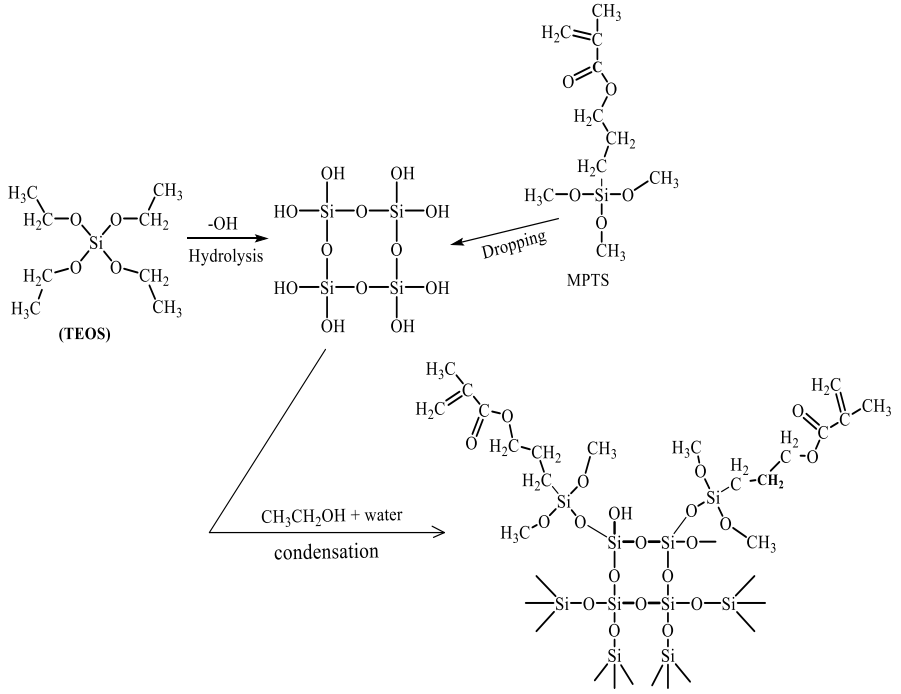

Finally, the inorganic constituent was added to the reflux flask containing the organic constituent. At this stage, the polymerisation products from the first and second stages were mixed at a temperature of 80 °C for 5 min to obtain the homogeneous hybrid solution used to coat the steel rebars [28].

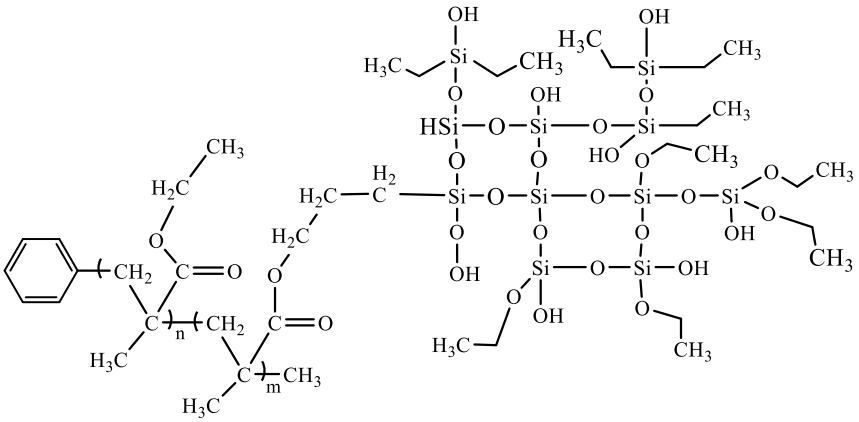

Carbon steel rebars were obtained in two sizes, that is, 10 mm diameter × 3 cm length, and 10 mm diameter × 10 cm length. Without knowing the chemical composition of the steel in advance, we lacked information about the proportions of elements used in its manufacture. Before coating, the bars were polished using silicon carbide sandpaper (iron paper) and cleaned in an ethanol ultrasonic cleaning for 15 min, before being dehydrated with nitrogen. The bars were immersed in a nitric acid solution for 5 min at 25 °C, cleaned with ethanol, and dehydrated again with nitrogen. In each hybrid polymer solution, the steel rebars were immersed for 1 min and then treated using the films obtained from the remaining hybrid polymer solution at 160 °C for 3 h to remove the solvent and complete the coating process. Figure 1 shows photographic images of several steel rebars coated with the hybrid monomers [30,31].

(a) (b)

FIGURE 1. Photographic images of several steel rebars coated with hybrid monomers (a) steel rebars size 10 mm diameter × 3 cm length,) steel rebar size 10 mm diameter × 10 cm length

RESULTS AND DISCUSSION

Table 1 and Figure 2, in addition to (Figures S1 and S2 in the Supplementary Information) present the normalised FT-IR spectra of the organic-inorganic hybrid polymers that were used to compare the FT-IR spectra of different BPO/EMA molar ratios. Figure 2 shows carbonyl group C=O stretching for W1 at 1718 cm^{-1}, the peak being slightly shifted at 1720 cm^{-1}, and conjugated with the double bond C=C at 1640 cm^{-1}, owing to the C=C of the aromatic ring of the initiator. The W2 and W3 samples exhibit peaks at 1720 cm^{-1} from the ester of the organic phase. Here, -CH_3 rocking, C-H bending, and C-O-C skeletal vibrations, exhibit distinct bands that were practically identical in all samples, that also applied to symmetrical and asymmetrical stretching; the peaks at 1086, 1054, and 898 cm^{-1} in the spectrum could be designated to the ethoxy Si–O–C_2H_5 group of TEOS and methoxy O-CH_3 groups of MPTS.

Additionally, the peaks at 1028, 1026, 936, 901, 898, 890, and 831 cm^{-1} could be attributed to the Si−O−Si stretching vibrations formed during the condensation and hydrolyzation processes. The TMPSM or inorganic phase exhibited many characteristic bands, attributable to Si−CH stretching vibrations at 784, 749, 705, and 701 cm^{-1}. The region between 2987 and 2901 cm^{-1} could be attributed to the C-H stretching vibrations for all samples, the CH_2 and CH_3 groups of TMPSM and PEMA, and the Si–OH related groups, which appeared as a result of the hydrolysis and condensation reactions [28,32–35].

TABLE 1. The primary peaks observed in the FT-IR spectra for organic-inorganic hybrid polymers.

Vibrational modes of the chemical bond	Sample W1 (0.33 g of BPO)	Sample W2 (0.66 g of BPO)	Sample W3 (1.32 g of BPO)
Carbonyl group (C=O) vibrations from the ester	1718 cm^{-1}	1720 cm^{-1}	1720 cm^{-1}
-CH_3 rocking, C-O-C skeletal vibrations, C-H bending	1453, 1393 cm^{-1}	1478, 1450, 1390 cm^{-1}	1478, 1450, 1390 cm^{-1}
C−O asymmetric stretching and Si−O−CH_2CH_3 symmetrical stretching	1251, 1054, 1086 cm^{-1}	1243, 1144, 1086 cm^{-1}	1223, 1143, 1086 cm^{-1}
Si-O^- groups of TEOS and groups of Si-O-Si peaks, which appeared later.	898 cm^{-1}	1028, 936,831 cm^{-1}	1026, 901, 890, 780 cm^{-1}
Si−CH stretching vibrations	784, 701 cm^{-1}	749, 705 cm^{-1}	749, 705 cm^{-1}
C-H stretching	2987, 2901 cm^{-1}	2983, 2901 cm^{-1}	2986, 2901 cm^{-1}
Si–OH groups	3745, 3672 cm^{-1} weak band	3740, 3372 cm^{-1} weak band	3742, 3672, 3543 cm^{-1} weak band

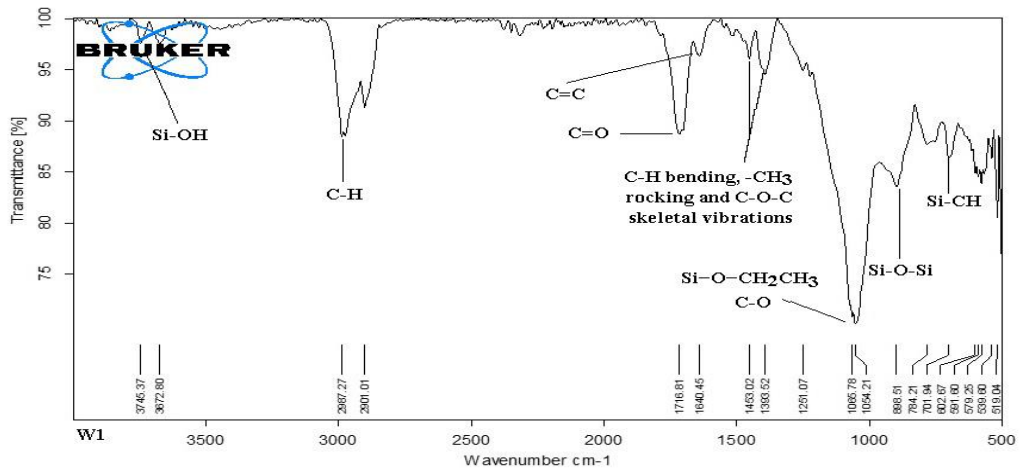

FIGURE 2. FT-IR spectra of the organic–inorganic hybrid polymer W1.

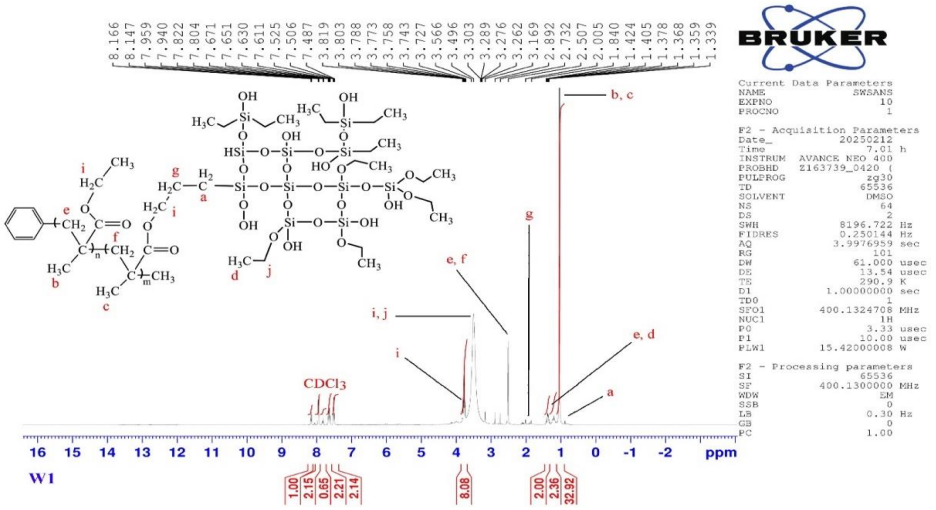

FIGURE 3. [1]HNMR spectra of the organic–inorganic hybrid polymer W1.

Figure 3, in addition to Figures S3 and S4 in the Supplementary Information, present the ^{1}H NMR spectrum and classified chemical structure of the hybrid polymer W1. Figure 3 shows that peaks observed at δ = 3.49 ppm (i) and δ = 3.30 ppm (i) and (j), owing to the protons of -COOC$\underline{H}_3$ and OC$\underline{H}_2$-. The proton peak of the -CH_2- groups observed at δ = 2.73 ppm (e) and (f), the proton peak of the -C$\underline{H}_2$- group observed at δ = 1.84 ppm (g), the proton peaks of the -C$\underline{H}_2$- and -C$\underline{H}_3$- groups (e), (d) observed at δ = 1.40 and δ = 1.42 ppm, respectively, the proton peaks of the -C$\underline{H}_3$ groups (b), (c) observed at δ = 1.37 ppm, and the proton peaks for groups related to the Si–O$\underline{H}$ groups (a) observed at δ = 1.33 ppm, owing to the hydrolysis and condensation reactions.

Figure S3 shows the ^{1}H NMR spectrum and classified chemical structure of the hybrid polymer W2. Figure S3 shows that the peaks observed at δ = 3.74 ppm (i) and δ = 3.52 ppm (i) and (j), owing to the protons of -COOC$\underline{H}_3$ and OC$\underline{H}_2$-. The proton peak of the -CH_2- group observed at δ = 2.50 ppm (e) and (f), the proton peak of the -C$\underline{H}_2$- group observed at δ = 1.80 ppm of the TMPSM (g), the proton peaks of the -C$\underline{H}_2$- and -C$\underline{H}_3$- groups (e), (d) observed at δ = 1.37 and δ = 1.36 ppm, respectively, the proton peaks of the -C$\underline{H}_3$ groups (b), (c) observed at δ = 0.88 ppm, and the proton peak for the Si–O$\underline{H}$ groups (a) that preceded it observed at δ = 0.87 ppm.

Finally, Figure S4 shows the ^{1}H NMR spectrum and classified chemical structure of the hybrid polymer W3. Figure S4 shows that the peaks observed at δ = 3.57 ppm (i) and δ = 3.38 ppm (i) and (j), owing to the protons of the -COOC$\underline{H}_3$ and OC$\underline{H}_2$- groups, the proton peak of the -CH_2- group observed at δ = 2.50 ppm (e) and (f), the proton peak of the -C$\underline{H}_2$- group observed at δ = 2.09 ppm of the TMPSM (g), the proton peaks of the -C$\underline{H}_2$- and -C$\underline{H}_3$- groups (e), (d) observed at δ = 1.43 and δ = 1.41 ppm, respectively, the proton peaks of the -C$\underline{H}_3$ groups (b), (c) observed at δ = 1.19 ppm, and the Si–O$\underline{H}$ related to groups (a) observed at δ = 0.86 ppm, owing to the hydrolysis and condensation reactions. The peaks observed could be accurately attributed to the chemical structures of the hybrid polymers W1, W2, and W3, indicative of their correct preparation.

Figure 4, in addition to Figures S5 and S6 in the Supplementary Information, show the ^{13}C NMR spectra used to identify the chemical hybrid structure of the polymer W1. Figure 4 shows that the peak of ester carbon (C=O) appeared at 167 ppm, whereas the vinyl carbon (C=C) peaks appeared between 128 and 135 ppm, owing to the carbon atoms of the initiator aromatic ring. These peaks also appeared in the FT-IR spectra, the ethoxy group (CH_3CH_2O) carbon peaks appearing at 62 ppm, the methyl carbon tied to the ethoxy group (C-C), appearing at 25 ppm, and the quaternary carbon peaks appearing at 40 ppm

The ^{13}C NMR spectra of the polymer W2 corresponded to the hybrid polymer W1, as shown in Figure S5. Here, the ester carbon atoms peak was absent, whereas vinyl carbon (C=C) peaks appeared between 129 and 130 ppm, for the same reason mentioned previously, which was the presence of carbon atoms in the initiator aromatic ring. The ethoxy group (CH_3CH_2O) carbon peaks appeared at 62 ppm, the methyl carbon tied to the ethoxy group (C-C), appeared at 25 ppm, and the quaternary carbon peaks appeared at 40 ppm.

Figure S6 shows the ^{13}C NMR spectra of the polymer W3. Here, the absence of the peak attributes with the ester C=O carbon atoms (170–180 ppm) suggests that the polymerisation was complete for all acrylates groups, However, cross-linking of the polymer could not be excluded. Vinyl carbon (C=C) peaks appeared between 129 and 130 ppm. The ethoxy group (CH_3CH_2O) carbon peaks appeared at 62 ppm, the methyl carbon tied to the ethoxy group (C-C) appeared at 25 ppm, and the quaternary carbon peaks observed at 39 ppm [36].

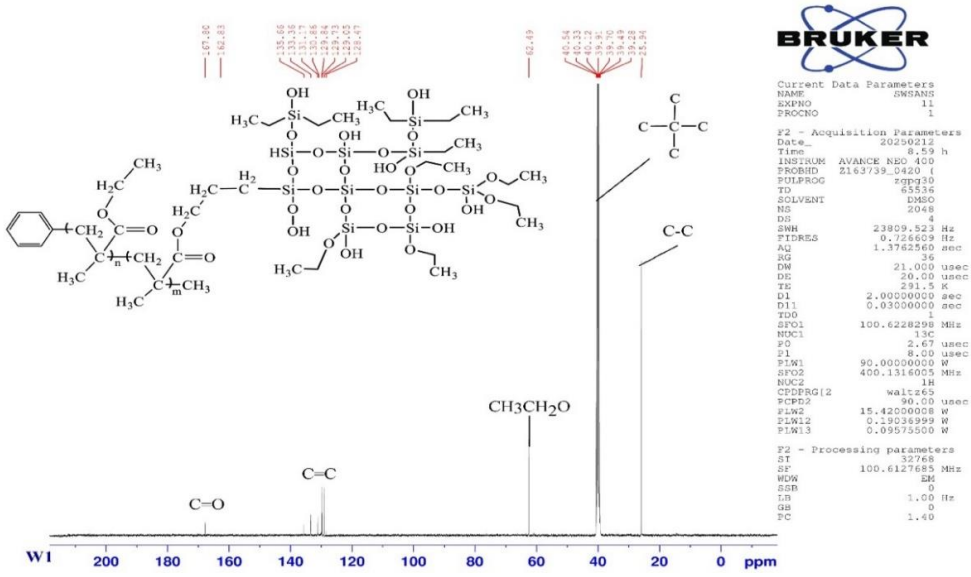

FIGURE 4. ^{13}CNMR spectra of the organic–inorganic hybrid polymer W1.

Figure 5, in addition to Figures S7 and S8 in the Supplementary Information, shows the degradation events of hybrid polymers in air. The TG and DSC curves were analysed to assess the thermal degradation, stability, and depolymerisation events in an oxidative atmosphere. The W1, W2, and W3 samples contained two phases—that is, the organic and inorganic phases. Thermal degradation of the organic phase was shown to be somewhat thermally stable (T_0) in the 25–250 °C range, with a mass loss of 13% for W1, 20% for W2 and 19% for W3. The weight lost within this range could be attributed to broken bonds, elimination of the remaining volatile molecules presented within the organic–inorganic hybrid sol-gel collection, and random depolymerisation. At 518 °C, the hybrid polymers were completely degraded, and a residue was formed by the silica and carbon charcoal [29,37,38].

Figure 5, in addition to the remaining figures in the Supplementary Information, show the DSC curves for the first heating cycles for all samples. Figure 5 shows that the endothermic step of the glass transition degree of the organic–inorganic hybrid polymer was detected between 37 and 100 °C, although precise determination of the glass transition degree was not possible using conventional DSC; however, using DTG curves (the first derivative of TG), through which it was possible to note the temperature range of individual steps, proved to be more valuable. Consequentlly, the exothermic step of the cold crystallisation peak (*Tc*) was located at a lower temperature, as the gas was released, this phenomenon takes place during curing reactions and is often concealed due to the simultaneous endothermic evaporation of minor gaseous substances, including the solvent and water.

The melting onset temperature (*Tm*) was determined to be 341, 302, and 365 °C, respectively, for all samples. Moreover, signs of the beginning of cross-linking appeared in samples W2 and W3, as shown by the endothermic peak before the thermal degradation events. Degradation appeared at a temperature of 400 °C, with complete degradation being reached at a temperature of 518 °C. For all samples, there were polymerisation defects, which confirmed the order of the polymer chains, owing to differences in the molar ratios of EMA/BPO, increasing initiator content, and the increase and decrease in the number of free radicals created from thermal decomposition [29,37,38].

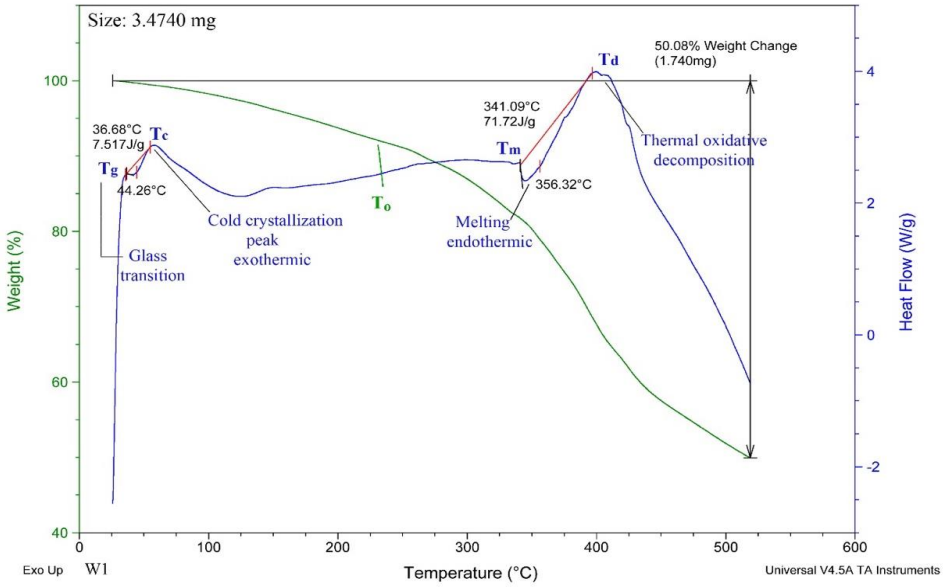

FIGURE 5. TG and DSC curves of the organic–inorganic hybrid polymer W1.

Figure 5, in addition to the remaining figures in the Supplementary Information, show the DSC curves for the first heating cycles for all samples. Figure 5 shows that the endothermic step of the glass transition degree of the organic–inorganic hybrid polymer was detected between 37 and 100 °C, although precise determination of the glass transition degree was not possible using conventional DSC; however, using DTG curves (the first derivative of TG), through which it was possible to note the temperature range of individual steps, proved to be more valuable. Consequentlly, the exothermic step of the cold crystallisation peak (*Tc*) was located at a lower temperature, as the gas was released, this phenomenon takes place during curing reactions and is often concealed due to the simultaneous endothermic evaporation of minor gaseous substances, including the solvent and water.

The melting onset temperature (*Tm*) was determined to be 341, 302, and 365 °C, respectively, for all samples. Moreover, signs of the beginning of cross-linking appeared in samples W2 and W3, as shown by the endothermic peak before the thermal degradation events. Degradation appeared at a temperature of 400 °C, with complete degradation being reached at a temperature of 518 °C. For all samples, there were polymerisation defects, which confirmed the order of the polymer chains, owing to differences in the molar ratios of EMA/BPO, increasing initiator content, and the increase and decrease in the number of free radicals created from thermal decomposition [29,37,38].

Figure 6 shows the SEM images used to examine the microstructure and thicknesses of the organic–inorganic hybrid polymers applied as a reinforced-steel coating. All sample films exhibited a similar appearance for the coating synthesised with molar ratios of the BPO/EMA and TEOS/TMPSM mixtures. SEM observations showed the formation of smooth, uniform, and crack free protective films, without visible pores or flaking. However, the hybrid film coatings exhibited some defects, that is, the emergence of silica aggregates on the film surfaces was evident. In general, all films exhibited similar appearances owing to the effect of the inorganic content in the hybrid polymer on the coating morphology [29,39,40].

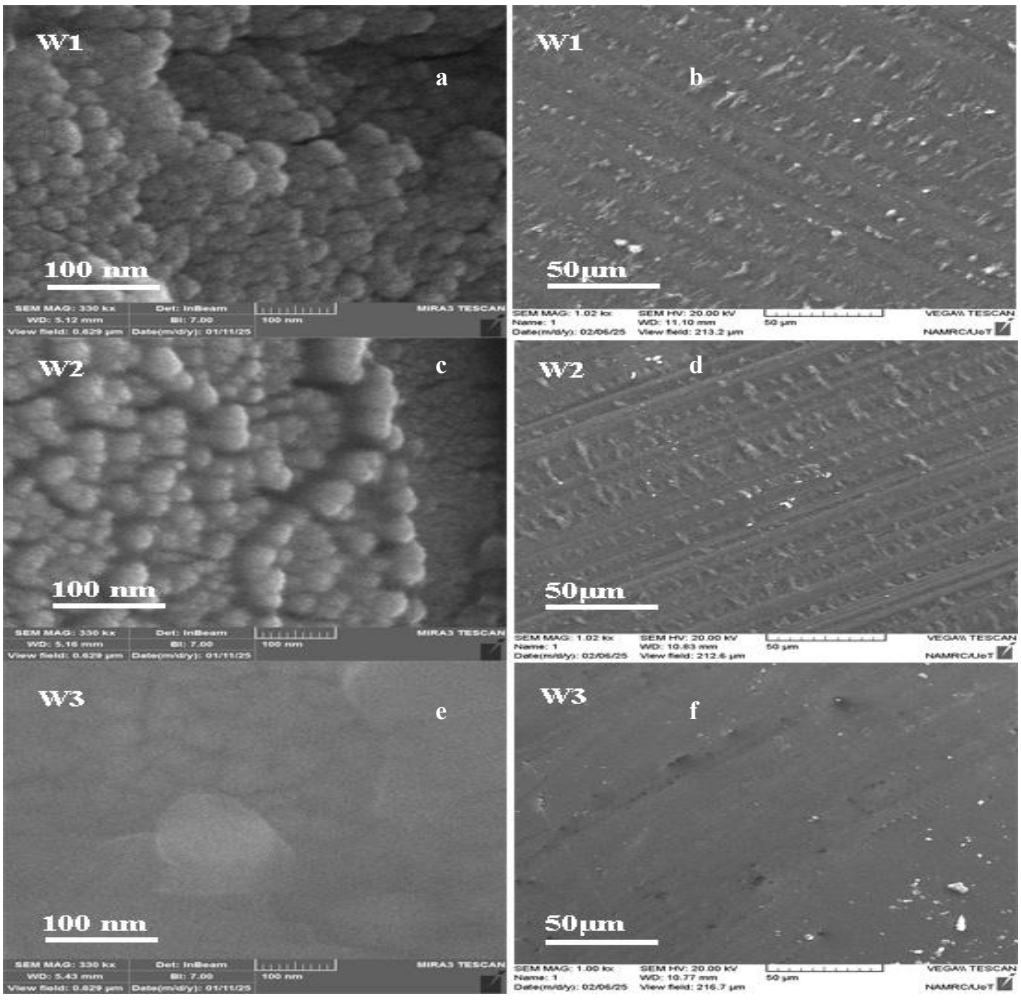

FIGURE 6a,b,c,d,e,f. SEM micrographs for the prepared hybrid coating films.

Figures 7(a), 7(b), 7(c) and 7(d), in addition to Figures S9 and S10 in the Supplementary Information, present topographical images obtained using AFM, recorded by scanning an area of 4.18 μm^2 (4180 nm). Figures 7(a) and 7(b) show the uniform morphology of the hybrid films and smoother surfaces with some areas containing small agglomerates, owing to the presence of a more condensed silica phase. However, no defects, cracks, pores, or inhomogeneities were evident on the coated samples, owing to the compatibility of the proportions used in the polymerisation reaction containing the organic and inorganic phases.

The thickness of the coating film of sample W1 was measured using a 3D profilometer, the thickness being 30 ±0.3 µm. As shown in Figure 7(c), the size of the silica particles in the histogram ranged from 0–23.28 nm. Moreover, Figure 7(d), shows that the mean diameter ranged from 0–200 nm. Generally, the reason for the size gradation of silica particles is their tendency to agglomerate within the polymer matrix. Moreover, the regularity of the surface corresponds to the atomic number of silica, specifically the atomic radius of silica in the polymer film. As these particles are the only ones that hybridise with the polymer, this means that the surface is topographically uniform at the atomic scale.

Figures S9 and S10 in the Supplementary information show that the other samples (W2 and W3) exhibited similar features to sample W1, the thickness of the coating film being 31 ±0.3 µm for both W2 and W3. The dimensions of

the silica particles in the histogram graded from 0–18.13 nm and 0–26.39 nm, respectively, and the mean diameter ranged from 0–175 nm and 0–250 nm, respectively [29,39,40].

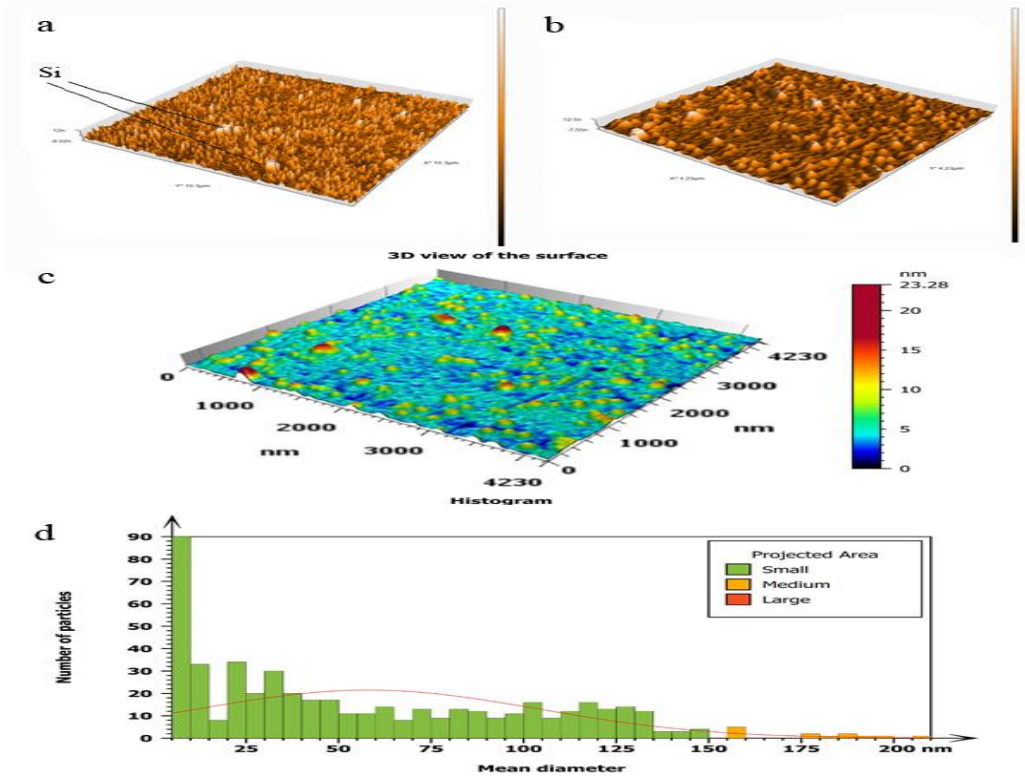

FIGURE 7. (a),(b) AFM images of the polymer film topography of sample W1. (c) 3D representation of a particle diagram, (d) average particle diameter.

CONCLUSIONS

In this study, we prepared coatings from hybrid monomers of EMA (as the organic phase) and silica in TMPSM and TEOS (as the inorganic phase) by changing the molar ratio of the thermal initiator—specifically, 0.025 (0.33g) for W1, 0.05(0.66g) for W2 and 0.1(1.32g) for W3—using ethanol as the solvent. These coatings were then positioned on steel rebars. The hybrid polymer coatings presented homogeneous surfaces, free from cracks and visible pores, and offered higher scratch resistance and improved adhesion to the steel rebars. FT-IR, NMR, TG, and DSC analyses revealed the formation of the hybrid polymer structures. It was evident that the best performing samples W2 and W3. These samples had acceptable thickness and contributed to prolonging the lifetime of the coatings. The TG and DSC analyses revealed that the samples had thermal stability up to 250 °C, and a highly cross-linked silica network. These results suggest that the W2 and W3 sample coatings represent an interesting alternative to conventional corrosion protection systems.

REFERENCES

1. M. P. Ryan, D. E. Williams, R. J. Chater, B.M. Hutton, and D.S. McPhail. Why Stainless Steel Corrodes. Nature. **415**, 770–774 (2002).

2. M. Betoya, T. Bojinov, K. Laitinen, P. Makela and T. S. Pohjanne. The transpassive dissolution mechanism of highly alloyed stainless steels: I. Experimental results and modeling procedure. Corros. Sci. **44**, 2675-2697 (2002).
3. Y. P. Virmani and G. G. Clemena, Corrosion Protection: Concrete Bridges. Report No. FHWA-RD-98-088, Federal Highway Administration, Washington DC. 1998.
4. Portland Cement Association. Corrosion of Embedded Metals. Retrieved from Portland Cement Association (2017) http://www.cement.org/learn/concrete-technology/ durability/ corrosion-of-embedded-materials.
5. M. G. Alexander, H. Beushausen and M. B. Otieno, Corrosion of steel in reinforced concrete: Influence of binder type, water/binder ratio, cover and cracking. Research Monograph No. 9. Collaborative research by the University of Cape Town and the University of the Witwatersrand (2012).
6. C. J. Brinker and G. W. Scherer, Sol-Gel Science: The Physics and Chemistry of Sol-Gel Processing. Academic Press. Boston (1990).
7. A. Arkhireeva, J. N. Hay, J. M. Lane, M. Manzano, H. Masters, W. Oware and S. J. Shaw. Synthesis of Organic-Inorganic Hybrid Particles by Sol-Gel Chemistry. J. Sol Gel Sci. Technol., **31**, 31-36 (2004).
8. M. L. Zheludkevich, L. M. Salvado and M. G. S. Ferreira. Sol-Gel Coatings for Corrosion Protection of Metals. J. Mater. Chem. **15**, 5099- 5111 (2005).
9. D. Álvarez, A. Collazo, M. Hernández, X. R. Nóvoa and C. Pérez. Characterization of hybrid sol–gel coatings doped with hydrotalcite-like compounds to improve corrosion resistance of AA2024-T3 alloys. Progress in Organic Coatings. **68**, 91-99 (2010).
10. P. Pepe, P. Galliano, M. Aparicio, A. Durán and S. Ceré. Sol-Gel Coatings on Carbon Steel: Electrochemical Evaluation. Surf. Coat. Technol., **200**, 3486–3491(2006).
11. K. Joncoux-Chabrol, J-P Bonino, M. Gressier, M-J. Menu and N. Pébère. Improvement of Barrier Properties of a Hybrid Sol-Gel Coating by Incorporation of Synthetic Talc-Like Phyllosilicates for Corrosion Protection of a Carbon Steel. Surf. Coat. Technol., **206**, 2884–2891 (2012).
12. R. B. Figueira, C.J.R. Silva and E.V. Pereira. Hybrid sol–gel coatings for corrosion protection of galvanized steel in simulated concrete pore solution. J. Coat. Technol. Res., **13**, 355–373 (2016).
13. S.V. Harb, A. Trentin, R.F.O. Torrico, S.H. Pulcinelli, C.V. Santilli, and P. Hammer. Organic-Inorganic Hybrid Coatings for Corrosion Protection of Metallic Surfaces. In New Technologies in Protective Coatings; Giudice, C., Canosa, G., Eds.; InTech. (2017) ISBN 978-953-51-3491-6.
14. S.R. Kunst, H.R.P. Cardoso, C.T. Oliveira, C.I. da Silva Filho, V.H.V. Sarmento, T.L. Menezes, I.L. Muller and C.D.F. Malfatti. Influence of Tetraethoxysilane Addition in Siloxane- Poly(Methyl Methacrylate) Hybrid Films Applied on Galvanized Steel. Int. J. Electrochem. Sci. **8**, 11984- 12004 (2013).
15. F.C. Santos, S.V. Harb, M-J. Menu, V. Turq, S.H. Pulcinelli, C.V. Santilli and P. Hammer. On the structure of high performance anticorrosive PMMA–siloxane–silica hybrid coatings. RSC Adv.**5**, 106754–106763 (2015).
16. M. Poberžnik, D. Costa, A. Hemeryck and A. Kokalj. Insight into the Bonding of Silanols to Oxidized Aluminum Surfaces. J. Phys. Chem. C**. 122**, 9417–9430 (2018).
17. M. Poberžnik and A. Kokalj. Implausibility of bidentate bonding of the silanol headgroup to oxidized aluminum surfaces. Appl. Surf. Sci. **492**, 909–918 (2019).
18. P. Rodič, R.C. Korošec, B. Kapun, A. Mertelj and I. Milošev. Acrylate-Based Hybrid Sol-Gel Coating for Corrosion Protection of AA7075-T6 in Aircraft Applications: The Effect of Copolymerization Time. Polymers. **12**, 948 (2020).
19. G. Kickelbick. Concepts for the incorporation of inorganic building blocks into organic polymers on a nanoscale. Prog. Polym. Sci. **28**, 83–114 (2003).
20. S.A. Pellice, R.J.J. Williams, I. Sobrados, J. Sanz, Y. Castro, M. Aparicio and A. Durán. Solutions of hybrid silica microgels as precursors of sol–gel coatings. J. Mater. Chem. **16**, 3318–3325 (2006).
21. Y. Wei, D. Yang and L. Tang. Synthesis, characterization, and properties of new polystyrene-SiO2 hybrid sol-gel materials. J. Mater. Res. **8**, 1143–1152 (1993).
22. Y. Abe, Y. Honda and T. Gunji. Preparation and properties of silicon-containing polymer hybrids from 3-methacryloxypropyltrimethoxysilane. Applied organometallic chemistry. **12**, 749–753 (1998).
23. J. Méndez-Vivar and A. Mendoza-Bandala. Spectroscopic study on the early stages of the polymerization of hybrid TEOS–RSi (OR′)3 sols. J. Non-Cryst. Solids **261**, 127–136 (2000).
24. M. Criado, I. Sobrados and J. Sanz. Polymerization of hybrid organic–inorganic materials from several silicon compounds followed by TGA/DTA, FTIR and NMR techniques. Progress in Organic Coatings **77**, 880–891 (2014).
25. W.J. van Ooij, D. Zhu, M. Stacy, A. Seth. T. Mugada, J. Gandhi and P. Puomi. Corrosion Protection Properties of Organofunctional Silanes—An Overview. Tsinghua Sci. Technol. **10**, 639-664 (2005).

26. M. Quinet, B. Neveu, V. Moutarlier, P. Audebert and L. Ricq. Corrosion protection of sol–gel coatings doped with an organic corrosion inhibitor: Chloranil. Prog. Org. Coat. **58**, 46-53 (2007).
27. A.A. El Hadad, V. Barranco, A. Jim´enez-Morales, E. Pe´on, G.J. Hickman, C.C. Perry and J.C. Galv´an. Enhancing in vitro biocompatibility and corrosion protection of organic–inorganic hybrid sol–gel films with nanocrystalline hydroxyapatite. J. Mater. Chem. B. **2**, 3886-3896 (2014).
28. A.R. Cho and S.Y. Park. Synthesis of titania- and silica-polymer hybrid materials and their application as refractive index-matched layers in touch screens. Optical Materials Express. **5**, 690-703 (2015).
29. M.C. Uvida, A. Trentin, S.V. Harb, S.H. Pulcinelli, C.V. Santilli and P. Hammer. Nanostructured Poly(methyl Methacrylate)−Silica Coatings for Corrosion Protection of Reinforcing Steel ACS Appl. Nano Mater. **5**, 2603−2615 (2022).
30. F.C. dos Santos, S.H. Pulcinelli, C.V. Santilli and P. Hammer. Protective PMMA-Silica Coatings for Aluminum Alloys: Nanostructural Control of Elevated Thermal Stability and Anticorrosive Performance. Prog. Org. Coat. **152**, 106129 (2021).
31. L.E. Manring. Thermal Degradation of Poly(Methyl Methacrylate). 2. Vinyl-Terminated Polymer. Macromolecules. **22**, 2673-2677 (1989).
32. L.M. Smith and M.L. Coote. Effect of temperature and solvent on polymer tacticity in the free-radical polymerization of styrene and methyl methacrylate. J. Polym. Sci. Pol. Chem. **51**, 3351–3358 (2013).
33. C. Zhang, L. Li, H. Cong and S. Zheng. Poly(methyl methacrylate)-block-poly(N-vinyl pyrrolidone) deblock copolymer: A facile synthesis via sequential radical polymerization mediated by isopropylxanthic disulfide and its nanostructuring polybenzoxazine thermosets. J. Polym. Sci. Pol. Chem. **52**, 952–962 (2014).
34. J. Du and Y. Chen. Atom-Transfer Radical Polymerization of a Reactive Monomer: 3-(Trimethoxysilyl)propyl Methacrylate Macromolecules. **37**, 6322–6328 (2004).
35. H. Wei, C. Cheng, C. Chang, W.Q. Chen, S.X. Cheng, X.Z. Zhang and R.X. Zhuo. Synthesis and Applications of Shell Cross-Linked Thermoresponsive Hybrid Micelles Based on Poly(N-isopropylacrylamideco- 3-(trimethoxysilyl)propyl methacrylate)-b-poly(methyl methacrylate). Langmuir. **24**, 4564–4570 (2008).
36. H.W.P. de Carvalho, A.F. Suzana, C.V. Santilli and S.H. Pulcinelli. Structure and thermal behavior of PMMA-polysilsesquioxane organic-inorganic hybrids. Polymer Degradation and Stability. **104**, 112-119 (2014).
37. R.B. Figueira, C.J.R. Silva and E.V. Pereira. Hybrid sol–gel coatings for corrosion protection of galvanized steel in simulated concrete pore solution. J. Coat. Technol. Res., **13**, 355–373 (2016).
38. A. Trentin, L. de, A. Gasparini, F.A. Faria, S.V. Harb, F.C. dos Santos, S.H. Pulcinelli, C.V. Santilli and P Hammer. Barrier properties of high performance PMMA-silica anticorrosion coatings. Progress in Organic Coatings. **138**, 105398 (2020).
39. M. Longhia, S.R. Kunstaa, L.V.R. Beltramib, E.K. Kerstnerb, C.I.S. Filhoc, V.H.V. Sarmentoc and C. Malfattib. Effect of Tetraethoxy-silane (TEOS) Amounts on the Corrosion Prevention Properties of Siloxane-PMMA Hybrid Coatings on Galvanized Steel Substrates. Materials Research. **18**, 1140-1155 (2015).
40. P. Hammer, F.C. dos Santos, B.M. Cerrutti, S.H. Pulcinelli and C.V. Santilli. Highly corrosion resistant siloxane-polymethyl methacrylate hybrid coatings. J Sol-Gel Sci Technol; **63**, 266–274 (2012).